Journal of Analytical and Applied Pyrolysis 194 (2026) 107542

Contents lists available at ScienceDirect

Journal of Analytical and Applied Pyrolysis

journal homepage: www.elsevier.com/locate/jaap

Mechanistic insights into slow pyrolysis of hydrothermal carbon

Luke J.R. Higgins [a],*, James M. Hammerton [b], Evangeline B. McShane [c], Andrew B. Ross [b], Christoph J. Sahle [d], Bhoopesh Mishra [e]

[a] Diamond Light Source, Harwell Science & Innovation Campus, Didcot, OX11 0DE, UK
[b] School of Chemical and Process Engineering, Woodhouse Lane, University of Leeds, Leeds, LS2 9JT, UK
[c] Department of Chemistry, Loughborough University, Loughborough, LE11 3TU, UK
[d] European Synchrotron Radiation Facility, Avenue des Martyrs, Grenoble, 38043, France
[e] Department of Physics, Illinois Institute of Technology, 10 West 35th St., Chicago, IL, USA

ARTICLE INFO

Keywords:
Hydrothermal carbonisation
Pyrolysis
X-ray Raman scattering
Pyrolysis GCMS

ABSTRACT

Slow pyrolysis of fructose-derived hydrothermal carbon spheres at temperatures between 200 °C to 600 °C has been investigated using X-ray Raman spectroscopy and pyrolysis gas chromatography-mass spectrometry in combination with infrared spectroscopy, elemental analysis and thermogravimetry. This study demonstrates the application of temperature resolved X-ray Raman spectroscopy to map the evolution of carbon functionality in complex organic materials. The results show that thermolysis of the polyfuranic linking units within hydrothermal carbon occurs between 300 °C to 350 °C. At pyrolysis temperatures above 350 °C, a stable C–O species is observed. The combination of X-ray Raman and pyrolysis GCMS is used in a synergistic approach to monitor both evolving pyrolysate chemistry and bulk carbon composition. The evolution of key furanic and aromatic analytes during pyrolysis is reported. This work contributes to our understanding of the thermal stability and reactivity of these materials, which is essential for optimising their applications as catalyst supports.

1. Introduction

Hydrothermal carbonisation (HTC) is a sustainable thermochemical process that converts wet biomass into valuable products: liquid platform chemicals and solid carbonaceous materials [1–3]. The liquid product, known as process water, contains important chemicals like levulinic acid and 5-hydroxymethylfurfural (5-HMF), which are crucial platform molecules for producing biomass-derived chemicals [4,5]. The solid product, hydrochar, can be used to create advanced carbon materials [6]. HTC is now considered one of the most sustainable technologies for upgrading biomass in a circular bioeconomy [7]. This article focuses on understanding the bulk carbon chemistry of secondary chars, and the pyrolysis of the stable polyfuranic carbon network they are composed of [8,9].

HTC-derived carbon materials have diverse applications, including catalyst supports and energy materials like supercapacitors and carbon anodes, typically using carbohydrate and lignocellulosic feedstocks [10–12]. For example, a HTC-derived Fe-N/C catalyst has shown high efficacy for electrocatalytic oxygen reduction as an alternative to noble metal catalysts [10]. Compared to slow pyrolysis, hydrothermal carbonisation (HTC) presents several advantages for carbon production. It operates at lower process temperatures, which may reduce electricity costs by up to 25% [13]. Moreover, HTC is compatible with feedstocks that possess high inherent moisture content, a common characteristic of biomass materials and waste biomass sources in particular. The process conditions also facilitate the incorporation of heteroatoms such as nitrogen, oxygen, and sulphur into the chemical structure of the carbon. The incorporation of such heteroatoms allows for greater flexibility in the design of tailored active sites by acting as nucleation sites for catalytically active species [14,15]. Additionally, HTC allows for a degree of control over the morphology and particle size of the resulting carbon material, a level of tunability that is generally not achievable through pyrolysis alone [16]. The aforementioned benefits have resulted in HTC becoming a successful technology for producing useful, low-cost sustainable carbon materials for a wide range of applications. However, to improve certain properties (e.g., low porosity, poor conductivity) of the raw HTC-derived carbon, a post-synthetic pyrolysis step is often required at temperatures between 400 °C to 1000 °C depending on the final application [11,17]. The value of a hybrid pyrolysis-hydrothermal (pyHTC) approach lies in the combination of the properties of HTC (e.g., heteroatom sites, morphology/size control, low energy synthesis) with further control over porosity, conductivity and the development

---

* Corresponding author.
E-mail address: luke.higgins@diamond.ac.uk (L.J.R. Higgins).

https://doi.org/10.1016/j.jaap.2025.107542
Received 25 April 2025; Received in revised form 28 November 2025; Accepted 5 December 2025

of catalytic metal sites on the carbon [16]. The secondary thermal treatment of hydrothermal carbon — typically conducted via pyrolysis at elevated temperatures — plays a critical role in enhancing the material's physicochemical properties, thereby expanding its practical utility. This post-treatment significantly increases the surface area and porosity of the carbon structure, which is essential for applications such as adsorption, catalysis, and energy storage, where high surface accessibility is crucial [18,19]. Additionally, pyrolysis improves the electrical conductivity of HTC-derived materials by promoting graphitisation and reducing the content of oxygen-containing functional groups. This enhancement is particularly beneficial for electrochemical applications, including supercapacitors, batteries, and electrocatalysts, where efficient charge transport is required [20]. Furthermore, the thermal treatment can stabilise catalytically active species on the surface, for example $M - N_4$ (M = metal) species have been shown to be highly favourable for a range of reactions [10]. In practical terms, post-synthetic treatment of hydrothermal carbons is now commonplace for improving the physicochemical properties of HTC and would likely be necessary for any real-world deployment. However, the use of a post-synthetic pyrolysis step comes with a significant energy and process complexity cost, as well as changes in chemical properties which may be undesirable. Therefore, it is essential to comprehensively understand the reaction pathway of pyHTC and monitor the bulk chemistry of the final product. This knowledge will enable the minimisation of energy costs and the systematic targeting of specific carbon functionality.

Due to the inherent complexities of non-graphitising carbon materials (e.g., multi-scale heterogeneity, high molecular weight, high optical absorption), methods for following bulk carbon and oxygen functionality are limited. Previous studies of the changes in physical properties of hydrothermal carbons have focussed on the increase in porosity and changes in surface properties [21]. Work using ^{13}C NMR spectroscopy has demonstrated that pyrolysis of model compounds results in the removal of the furan-type carbon species known to compose the bulk local structure of hydrothermal carbon [9,22]. However, the low abundance of ^{13}C and the difficulty in performing *in situ* measurements limit the information available from NMR. Similarly, X-ray spectroscopy approaches for studying low-Z materials require surface sensitive, low-energy, soft X-rays (e.g., XPS, NEXAFS) which must be performed in vacuum conditions and present significant challenges for utilising *in situ* sample environments. A relatively new approach to studying these materials is X-ray Raman scattering (XRS) spectroscopy, which enables the measurement of core electron transitions of low-Z elements, including carbon and oxygen using hard X-rays (ca. 10 keV). The use of XRS spectroscopy has many benefits for studying complex organic materials compared to other approaches (e.g., NMR, XPS, EELS), including the straightforward implementation of sample environments such as furnaces and bulk chemical sensitivity. These benefits are discussed in more detail elsewhere [23,24].

This study employs a combination of XRS and pyrolysis gas chromatography mass spectrometry (pyGCMS), in combination with elemental analysis, infrared spectroscopy and thermogravimetry to investigate the bulk local structure of hydrothermal carbon during pyrolysis. PyGCMS has been previously used to successfully examine the structural units within biomass-derived hydrothermal carbon [25–28]. PyGCMS facilitates the identification of evolved gas-phase pyrolysate species, thereby enabling the tracking of pyrolysis chemistry across different materials. The synergistic integration of pyGCMS and XRS in this study allows for a comprehensive analysis of both gas-phase and bulk solid-phase chemical transformations occurring during pyrolysis of HTC, which has not been accessible in previous work. Specifically, XRS provides higher-resolution spectroscopic information than ^{13}C-NMR for the furanic species which are the primary component of HTC and can be used for *in situ* measurements. This manuscript presents the first application of these techniques in tandem, combining PyGCMS and XRS to resolve changes in carbon and oxygen functionalities at known temperature transitions.

2. Experimental

2.1. Preparation of carbons

2.1.1. Fructose derived hydrothermal carbon

D(-)-Fructose ($\geq$ 99%) was obtained from Merck UK Ltd. Hydrothermal carbonisation was performed using 20 mL of an aqueous 10 % (v/v) fructose solution, loaded into a glass liner within a modified 600 mL benchtop autoclave (Parr, USA). Once sealed, the reactor was heated using a resistance jacket (5 °C min^{-1}) to 200 °C under autogenous pressure, then held for 12 h before the reactor was allowed to naturally cool to room temperature. The resulting solid was recovered by filtration without a solvent wash, then dried at 60 °C until the total mass had stabilised. Hydrothermal carbon yield was calculated as the quotient between the masses of the recovered carbon and the initial feedstock on a dry basis, with the yield being 58.6 %.

2.1.2. Thermal treatment

Pyrolysis of the produced hydrothermal carbon was performed in a modified vertical tube reactor at 200 °C to 600 °C and a ramp rate of 5 °C min^{-1} under flowing dry nitrogen gas (BOC N2.0, 130 mL min^{-1}) for a hold time of 1 h. Further details of the pyrolysis reactor may be found in the supplementary information (Figure S1) and in *Hammerton et al.* [29]. Pyrolysed fructose-derived hydrothermal carbon are labelled as pyHTC-XXX where XXX represents the temperature of the thermal treatment in Celsius.

2.2. Analytical techniques

2.2.1. X-ray Raman spectroscopy

XRS spectroscopy at the Carbon and Oxygen K-edges (285 eV, 530 eV) was performed using the large solid angle spectrometer at beamline ID-20 using undulator radiation at the ESRF [30]. A combination of a Si (111) high heat load monochromator and a Si (311) channel cut post-monochromator were used. Scattered photons were collected using 72 spherically bent Si (660) crystal analysers arranged in 6 arms containing 12 analyser crystals and a MAXIPIX 2D area detector each. Spectra were collected by scanning the incident energy between 9.9639 keV to 10.0239 keV (300 steps, 5 s dwell) for carbon and 10.2089 keV to 10.2689 keV (300 steps, 7 s dwell) for the oxygen K-edge with a fixed analyser energy of 9.6889 keV. The beam was defocussed to an approximate size of 100 x 80 μm (H x V) using a toroidal Kirkpatrick-Baez optical system. Samples were prepared as 6 mm pressed pellets and measured in grazing geometry at angle of 5°. Multiple spectra were collected at different points along the pellet, checked for consistency, and averaged to reduce the average time of the beam on one point. Uncertainties are based on Poisson counting statistics and are shown as 2σ confidence intervals in the figures. Full details regarding the spectrometer design at ID-20 can be found elsewhere [30]. Background subtraction of the energy-loss spectra was carried out in IXStools using parametrised Pearson VII functions guided by Hartree–Fock calculated core atomic potentials [31]. Peak fitting of carbon K-edge X-ray Raman spectra was performed using the LMFIT software [32]. Gaussian peak fitting has been widely used for NEXAFS data to follow changes in key features; in particular, peak fitting at the carbon K-edge is very commonly applied [33–38]. Gaussian peak fitting has also been used for fitting XRS data [23,39,40]. In this work, we follow the approach set out by *Stohr et al.* [33,41]. The carbon K-edge fitting utilised a series of Gaussian peaks initialised with a fixed transition energy from literature values (Table 2), and a variable intensity and full width half maximum (initially set to the experimentally observed energy resolution: 0.67 eV). Further details on the Gaussian fitting performed here can be found in the supplementary information.

2.2.2. Pyrolysis GCMS

0.8 mg of fructose hydrothermal carbon was loaded into quartz tubes with deactivated quartz wool at both ends. A CDS Analytical Ltd. 5200 pyroprobe instrument was used to pyrolyse the sample from room temperature to set temperatures (200, 300, 350, 400, 500, 600 °C) for 1 h under flowing dry N_2 gas (BOC N2 grade) at a rate of 5 °C min^{-1} mirroring the pyrolysis performed in 2.1.2. All measurements were performed in duplicate. The evolved gases were trapped on a Tenax sorbent tube and desorbed at the end of the pyrolysis temperature program. Fructose hydrothermal carbon was also subjected to fast pyrolysis at 500 °C with a heating rate of 20 °C ms^{-1} to fragment the material into the key components. The pyroprobe instrument was connected via heated transfer line (300 °C) to a Shimadzu GCMS-QP2010 SE. The column used was a 60 m RTX-5, the split ratio was set to 20:1 and the injector port was kept at 300 °C. The column oven temperature was initially 40 °C for 2 min then increased to 300 °C at 5.0 °C min^{-1} and held for 14 min. A diagram of the pyrolysis GCMS instrumentation is provided in the supplementary information (Figure S2). Analytes were identified by cross-reference with the National Institute of Standards and Technology (NIST 2020) mass spectral library using a minimum match quality of 97%.

2.2.3. Fourier transform infrared (FTIR) spectroscopy

Attenuated total reflectance-Fourier transform infrared (ATR-FTIR) spectroscopy was performed on a Nicolet iS-10 IR spectrophotometer using a diamond crystal. Samples were prepared by ball milling and measured as a neat powder. Qualitative analyses were performed over 400 cm^{-1} to 4000 cm^{-1} with 32 scans per sample. Background noise was subtracted from the sample runs using a spline function for each data set to normalise over the 700 cm^{-1} to 1800 cm^{-1} range.

2.2.4. Thermogravimetric and elemental analysis

Thermogravimetric analysis (TGA) was performed using a Mettler Toledo TGA/DSC 1 analyser with ca. 10 mg of sample, a heating rate of 1 °C min^{-1} and a maximum temperature of 650 °C under 50 mL min^{-1} of He (BOC) in platinum crucibles. TGA measurements were performed in duplicate. Elemental (C, H, N, S) and O analyses were performed using a FLASH-EA2000 elemental analyser fitted with an auto-sampler and thermal conductivity detector (Thermo Scientific). The FlashSmart elemental analyser (Fisher Sci.) used He as a carrier gas (BOC; CP Grade), with flow rates of 140 mL min^{-1} (sample side) and 100 mL min^{-1} (reference side). For CHNS analysis 1.5 mg to 2.5 mg of sample was pressed into tin capsules and analysed using a pre-packed CHNS oxidation/reduction reactor (CE Instruments Ltd) with oxygen as the oxidising gas (BOC; Grade N5.0) at a temperature of 900 °C. Oxygen analysis was performed with 2 mg to 3.5 mg of sample in silver capsules and analysed using a pre-packed pyrolysis reactor (Elemental Microanalysis Ltd) at a temperature of 1050 °C. Both CHNS and Oxygen analyses were performed in triplicate with analytical standards. Sulphur analyses were found to be below the instrument detection limits and are not reported here.

3. Results and discussion

3.1. Elemental and thermogravimetric analysis

The Van Krevelen diagram in Fig. 1 shows significant changes in the ratio of O:C within pyHTC as a function of pyrolysis temperature. These changes appear to be primarily driven by condensation reactions which are observed in the thermogravimetric analysis as a 33 ±5% mass loss during pyrolysis at 600 °C. It is also observed that there is a significant drop in O:C ratio between 300 °C to 400 °C (see Table 1). The results agree with other studies that have investigated similar changes in hydrothermal carbon, all of which show a significant mass loss between 350 °C to 450 °C [21,42]. Other studies have demonstrated using gas adsorption studies measurements that pyrolysed hydrothermal carbons show a relatively low porosity for the low-temperature treated carbons which increases upon higher temperature pyrolysis treatments [21,39]. In biomass-derived carbons, the inflection point at ca. 450 °C is due to the cracking of C–C bonds [43].

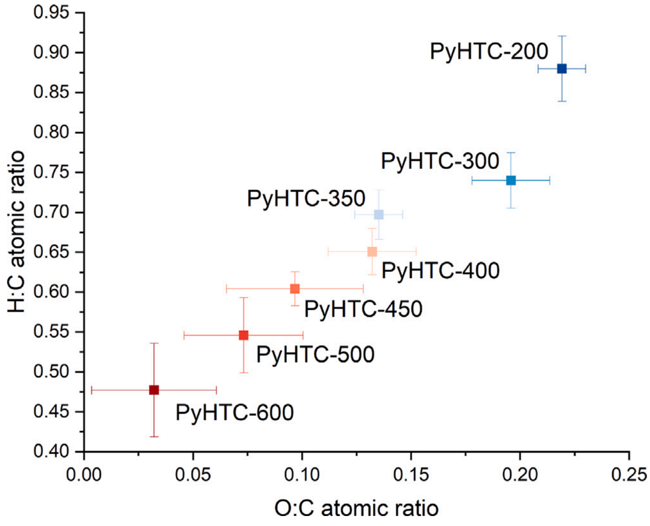

Fig. 1. Van Krevelen diagram for pyHTC between 200 °C to 600 °C from elemental (CHNS and O) analysis.

Table 1
Elemental analysis of pyHTC samples.

Sample	C (%)	H (%)	N (%)	O (%)	H:C	O:C
pyHTC-200	53.84	3.98	0.00	15.72	0.88(4)	0.22(1)
pyHTC-300	54.39	3.38	0.00	14.19	0.74(3)	0.19(2)
pyHTC-350	69.76	4.08	0.15	12.57	0.69(3)	0.13(1)
pyHTC-400	67.94	3.71	0.14	11.97	0.65(3)	0.13(2)
pyHTC-450	63.91	3.24	0.17	8.23	0.60(2)	0.09(3)
pyHTC-500	57.42	2.63	0.15	5.60	0.55(5)	0.07(3)
pyHTC-600	59.44	2.38	0.16	2.55	0.48(6)	0.03(3)

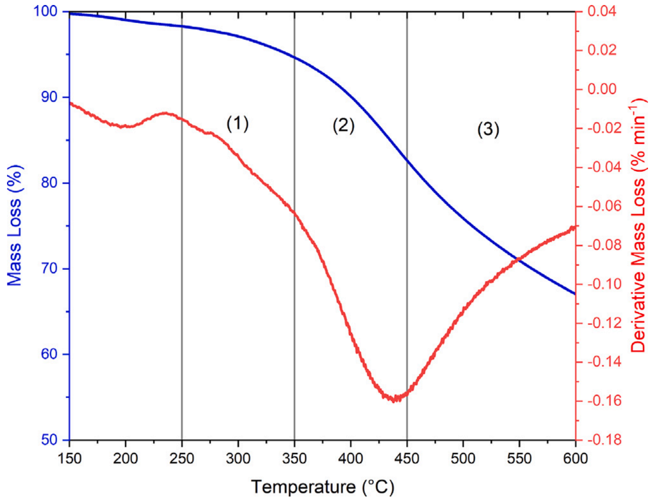

Fig. 2. Thermogravimetry for pyHTC between 150 °C to 600 °C.

The differential thermogravimetry curve in Fig. 2 shows three relevant regions of mass loss in the thermosequence: (1) between 250 °C to 350 °C, (2) between 350 °C to 450 °C and (3) 450 °C to 600 °C. These regions are proposed to be due to (i) the removal of volatile surface species (ii) the thermolysis of the polyfuran network and (iii) the condensation and aromatisation of the remaining carbon respectively. The inflection point in the differential TGA curve occurs at ca. 400 °C to 450 °C and is most likely due to the thermolysis of the polyfuran network, resulting in the removal of C–O bonds.

3.2. pyGCMS

Pyrolysis gas chromatography mass spectrometry (pyGCMS) was used to fragment hydrothermal carbon into smaller volatile fragments (pyrolysate), representing the structures present in the high molecular weight polymer structure. The pyroprobe instrument gives a great deal of control over the pyrolysis heating rate and flow delivery of the pyrolysate to the GCMS, which enables both slow and fast pyrolysis to be performed with accurate temperature control and fast ramp rates.

3.2.1. Fast pyrolysis

During fast pyrolysis (500 °C, 20 °C ms^{-1}), the pyrolysate (gas phase) was mainly composed of furans, lactones and cyclopentanones/enones (supplementary information) [44]. Cyclopentanones/enones present in hydrothermal carbon (e.g., 3-M-2-cyclopenten-1-one) were likely formed by ketonisation of organic acids, rearrangement of the polyfuranic structure, and oxidation of lactones, which form during HTC and have been detected both in the formed carbon, but also in the process water [45,46]. A study of the aqueous fraction (process water) produced during hydrothermal carbonisation also confirmed the presence of the species observed here during fast pyrolysis GCMS, notably cyclopentanones/enones and benzofurans [47]. Several oxygenated aromatic fragments were also detected during fast pyrolysis of the parent fructose-derived hydrothermal carbon, the most significant of which was 3-phenylbut-2-enal. Aromatic species are likely formed during condensation reactions, although it is possible that more aromatic fractions may exist as a non-volatile, higher molecular weight oil undetectable by GCMS. Present in smaller concentrations were phenol, acetophenone and 2,4,5-trimethylbenzaldehyde. Table S2 in the supplementary information contains a list of the retention times observed for chromatogram peaks and their corresponding assignments. In general, the fast pyrolysis GCMS results show that hydrothermal carbon is primarily formed of a furanic motif, with some organic acid and aldehyde sites present either as part of the bulk structure, or as physicochemically bound species (e.g., levulinic acid) [21].

3.2.2. Slow pyrolysis (250 °C to 350 °C)

In addition to fast pyGCMS, slow pyGCMS (5 °C min^{-1}) was conducted to replicate the thermal treatment applied in the preparation of pyrolysed hydrothermal carbon. The individual chromatograms for each pyrolysis temperature are available in S1.1, as well as a list of retention times and assignments for the observed chromatogram peaks (Table S1). Peak areas were normalised to the maximum value for each individual compound to enable clear comparison of temperature-dependent release profiles, as absolute concentrations varied by up to an order of magnitude between different analytes. Slow pyrolysis is known to favour the formation of solid carbons with condensed aromatic functionalities [48]. In this context, slow pyrolysis is more pertinent, and thus the pyroprobe heating conditions were designed to mimic those used in the production of pyHTC. Consequently, the pyrolysate is presumed to represent the volatile products generated during the thermal treatment of hydrothermal carbon, allowing for a comparative analysis between the pyrolysate and the bulk carbon. Results of the slow pyrolysis thermosequence are shown in Fig. 3. During the first stage of thermal treatment between 200 °C to 300 °C, 2-acetylfuran and lactones were the main compounds detected by slow pyGCMS. In this temperature range, around 40% of the maximum peak area detected in any of the slow pyrolysis experiments was released (Fig. 3a). Between 200 °C to 300 °C the pyrolysis temperature had little impact on the peak area of evolved 2-acetylfuran and lactones. This suggests that these compounds are only loosely bound to the hydrothermal carbon and are released once the temperature is increased above their boiling points, which are between 160 °C to 200 °C. Most likely, compounds such as angelica-lactone and γ-valerolactone are formed as derivatives of levulinic acid, which is known to form during hydrothermal carbonisation of fructose as a product of the rehydration of HMF [47]. Levulinic acid has also been detected by pyrolysis-FTIR as a pyrolysate product from carbohydrate-derived hydrothermal carbon [21]. These results suggest that levulinic acid remains adsorbed to the surface of the hydrothermal carbon, with other lower molecular mass furanic species.

3.2.3. Slow pyrolysis (350 °C to 400 °C)

An increase in furan and cyclopentanones/enones are released between 300 °C to 400 °C as the structure undergoes depolymerisation (Fig. 3a). Further lactones were produced in this range. These are likely formed as part of the pyrolysis process at these temperatures, as well as being present in the original structure. Between 300 °C to 400 °C the formation of both aromatic and furanic pyrolysis begins (Fig. 3b,c). The concentration of furanic analytes liberated during pyrolysis exhibits an earlier onset when compared to the selected aromatic analytes, with the majority of aromatic components liberated at temperatures >400 °C. The concentration of aromatic analytes seems to be directly correlated with temperature, whilst there is a noticeable ‘step increase’ in the concentration of furanic analytes which occurs at ca. 350 °C. This sudden increase in the concentration of removed furanic analytes corresponds with a change in O:C ratio observed in the Van Krevelen diagram Fig. 1. Beyond 400 °C there is a quasi-linear increase in the concentration of small aromatic (e.g., Toluene) species detected (Fig. 3b). These are likely produced by ring-opening and deoxygenation of furanic compounds [45].

3.2.4. Slow pyrolysis (400 °C to 600 °C)

Some aromatic fragments were released at all pyrolysis temperatures from slow pyrolysis indicating that these are produced during the hydrothermal carbonisation process. These fragments were released steadily as the pyrolysis temperature was increased. The most significant fragment detected was 3-phenylbut-2-enal, which consists of a benzene ring attached to a ring-opened furan. 2-methylbenzofuran was another significant aromatic fragment detected in all pyGCMS samples. This analyte has been previously reported to be present in process water samples [1,4]. Both fragments provide insight into how aromatic carbon forms during hydrothermal carbonisation. 2-methylbenzofuran was most likely formed via Diels–Alder reactions of two furanic compounds. The formation of 2-methylbenzofuran by this mechanism could occur during hydrothermal carbonisation or pyrolysis [49]. The presence of 3-phenylbut-2-enal suggests electrophilic aromatic substitution with furanic compounds at the β position, followed by ring-opening. The formation of C6 aromatics species (i.e., catechol, methylphenol, toluene) in the slow pyGCMS increases significantly above 400 °C, and were undetectable below 300 °C. Suggesting that C6 aromatic species are only formed during thermolysis of the polyfuran network.

3.3. FTIR of pyHTC product

FTIR has been widely performed on carbohydrate-derived hydrothermal carbons and some easily recognisable bands are present in the FTIR region between 800 cm^{-1} to 1800 cm^{-1}: (i) characteristic peak of C–O deformation in furan rings at 1020 cm^{-1} (ii) C=O stretch at 1700 cm^{-1} (iii) C=C stretch at 1600 cm^{-1} (iv) C=O stretch for aldehyde furfural groups at 1510 cm^{-1} (v) C-H vibration ca. 800 cm^{-1} (vi) 1200 cm^{-1} broad band, carboxylic acid C–OH stretch, O–H deformation [21,50,51].

Fig. 4 shows the ATR-FTIR spectra for pyHTC after pyrolysis between 200 °C to 600 °C. The two features at 1700 cm^{-1} and 1600 cm^{-1} are evidence of the presence of carbonyl group stretching in the furan structure and aromatic units respectively [52,53]. The removal of furan functionality with increasing pyrolysis temperature can be compared against the feature at 1600 cm^{-1}. The largest reduction in the 1700 cm^{-1}

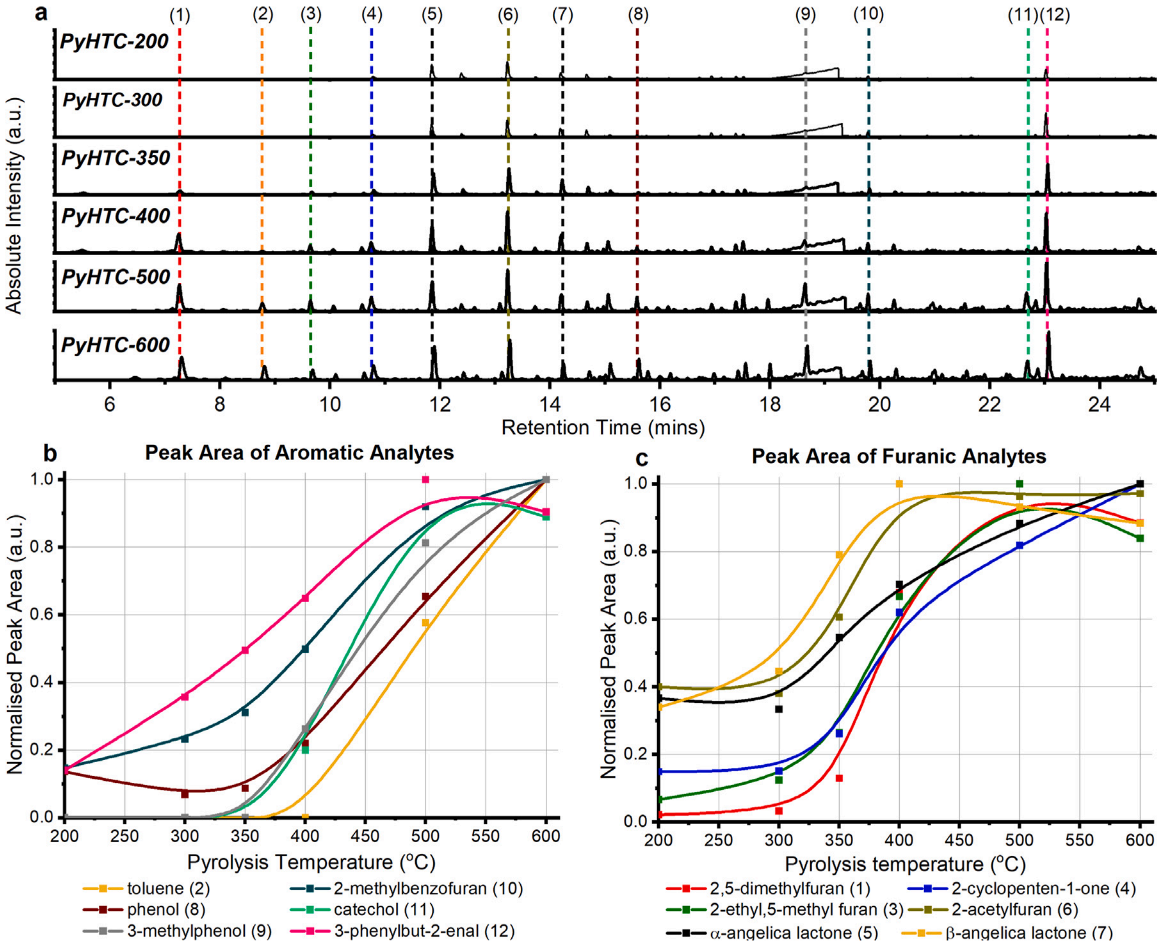

Fig. 3. (a) Slow pyGCMS chromatograms of fructose hydrothermal carbon produced at 250 °C for 12 h. All chromatograms are shown at the same scale. Labelled are key analytes identified by mass spectrometry across the thermosequence (200 °C to 600 °C). (1) 2,5-dimethylfuran, (2) toluene, (3) 2-ethyl,5-methylfuran, (4) 2-cyclopenten-1-one, (5) *α*-angelica lactone, (6) 2-acetylfuran. (7) *β*-angelica lactone, (8) phenol, (9) 3-methylphenol, (10) 2-methylbenzofuran, (11) catechol, and (12) 3-phenylbut-2-enal. (b) Normalised peak areas for detected aromatic pyrolysates. (c) Normalised peak areas for detected furanic pyrolysates.

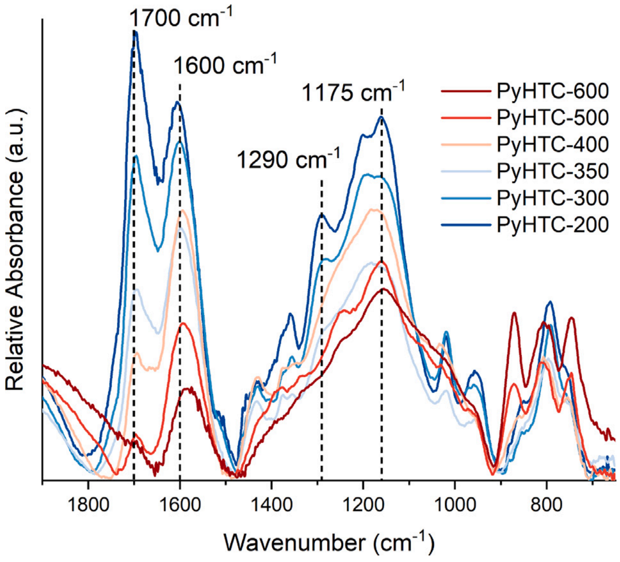

Fig. 4. ATR-FTIR spectra collected for pyHTC between 200 °C to 600 °C. A background spline has been subtracted over the 1800 cm^{-1} to 700 cm^{-1} to normalise the results.

C=O stretch occurs between 300 °C to 350 °C, the feature is totally removed by 600 °C. Other features in the FTIR spectra that are indicative of furanic structure are present at both 1510 cm^{-1} and 1020 cm^{-1}. These furan-related bands are almost totally removed by 350 °C, confirming decomposition of the polyfuran structure at this temperature. The decomposition of the polyfuran network is also evidenced by both the thermogravimetric analysis and pyGCMS. C–O skeletal bonds of secondary alcohols occurs as a stretch at 990 cm^{-1} [25]. Increasing the pyrolysis temperatures removes these functionalities, whereupon removal occurs between 300 °C to 350 °C. There are also noticeable changes in the C-H region at the 800 cm^{-1} region, with a triplet forming at higher temperatures, possibly due to increased amounts of aromatic functionalities.

3.4. X-ray Raman spectroscopy (XRS)

Previous investigations of the carbon *K*-edge using X-ray Raman Spectroscopy (XRS) and soft X-ray absorption spectroscopy (NEXAFS) have identified four key transitions in hydrothermal carbon spectra: aromatic, furan, aliphatic, and carboxyl functionalities (Table 2) [24, 34,35]. These transitions serve as markers to track the evolution of carbon speciation during pyrolysis of carbohydrate-derived hydrothermal carbon.

Fig. 5a shows collected XRS data for the recovered pyHTC at temperatures between 200 °C to 600 °C. The initial hydrothermal carbon, measured at room temperature, is shown in black. The most significant

Table 2
Key electron transition energies used in the analysis of collected XRS carbon *K* edge spectra.

Energy (eV)	Functional Interpretation	Transition
285.0	C═C aromatic	$1s - \pi^*$
286.6	C═C–O furan	$1s - \pi^*$
287.6	C–O phenolic, C–C aliphatic	$1s - \pi^*$, $1s - \sigma^*$
288.6	C═O-OH carboxyl/aldehyde	$1s - \pi^*$
292.0	C═C aromatic	$1s - \sigma^*$

feature in the initial carbon XRS spectrum is the C–O furan transition at 286.6 eV [24]. The relatively intense C–O furan transition in the spectrum is due to the structure of carbohydrate-derived hydrothermal carbon being composed of an interlinked polyfuranic network. This description of a polyfuranic network in carbohydrate-derived hydrothermal carbon has been previously reported and is evidenced by the range of furanic functionalities produced during fast pyrolysis (Section 3.2) [21,22,39].

The region between 283 eV to 290 eV (Fig. 5a, outlined in magenta), was used to generate a map of carbon functionality in the solid product after pyrolysis at temperatures corresponding to those of the performed PyGCMS (Fig. 5b). In this case, tracking the relative intensity of the transitions of known moieties was performed using a Gaussian fitting approach that has been widely used for NEXAFS analysis, but more recently in XRS datasets including those for complex organic matrices [23,24,40]. A series of Gaussian transitions (Table 2) were used to monitor known transitions in the selected energy region. The relative intensity of these Gaussians are shown in Fig. 5c. Further details of the Gaussian fitting methodology used here to semi-quantitatively monitor relative changes in carbon functionality in the bulk hydrothermal carbon between 200 °C to 600 °C can be found in the supplementary information. The error bars presented in Fig. 5c represent the combined error found from the fit and the experimental data.

3.4.1. 250 °C *to* 300 °C

An initial increase in aromatic peak area is observed at 200 °C, which does not change significantly as the pyrolysis temperature reaches 300 °C. The initial increase in aromatic peak area is mirrored in the furanic peak area, which ceases to change at 200 °C and stays stable until 300 °C. Aromatisation was not expected at a low-temperature regime (<300 °C). However, these changes can be explained by the initial removal of volatile organic species, as detected by slow pyGCMS, and the removal of aryl-like linking units.

3.4.2. 300 °C *to* 400 °C

In the temperature range of 300 °C to 400 °C, the pyrolysed material exhibits a significant decrease in the fitted furan peak area (Fig. 5c). Concurrently, there is an observed increase in both aromatic and aliphatic peak areas, attributed to the formation of double-bonded carbon species that subsequently undergo condensation reactions. Additionally, a step-wise reduction in carboxyl functionality is noted within this temperature interval, indicating the removal of these functionalities from the carbon surface. The disappearance of this shoulder in the thermosequence spectra (Fig. 5a) suggests that aromatisation progresses from the surface to the core, as carboxyl species are known to be enriched at the hydrothermal carbon surface [8]. This temperature range does not align with the peak mass-loss region observed in the thermogravimetry data (Section 3.1), implying that the material predominantly remains polymeric. This is supported by the pyGCMS data, which reveals that the majority of volatilised species are of higher molecular weight. The thermosequence map (Fig. 5b), in combination with the pyGCMS and thermogravimetric data indicates that the polyfuran network undergoes condensation at ca. 450 °C.

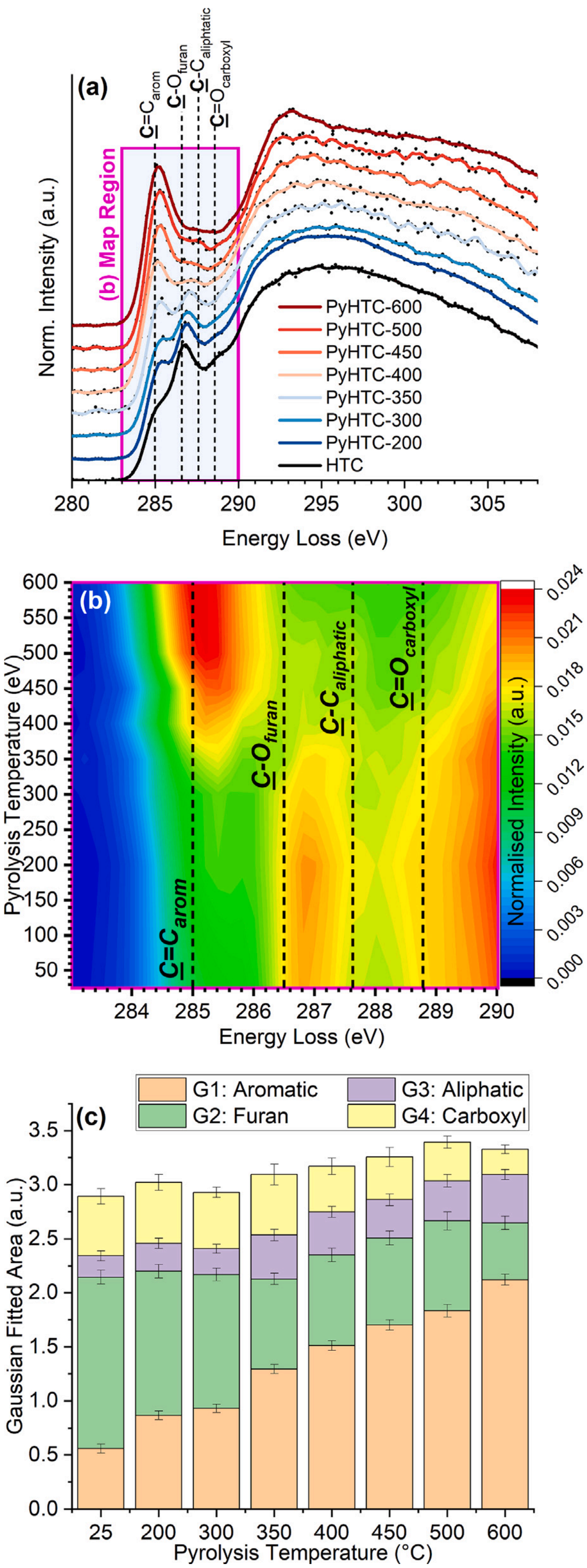

Fig. 5. (a) C *K*-edge XRS for thermosequence from room temperature (HTC) to pyHTC between 200 °C to 600 °C (b) normalised XRS spectra at selected temperatures with the energy region highlighted in magenta in (a). (c) Gaussian fitting results for key functionalities.

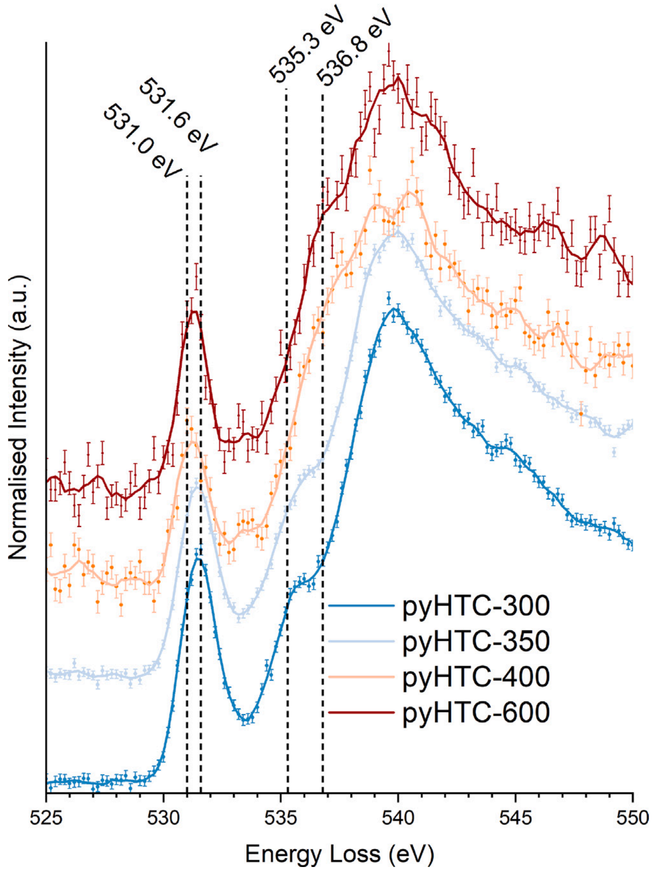

Fig. 6. O *K*-edge XRS of pyHTC between 300 °C to 600 °C. Key transition regions are highlighted by dashed lines.

3.4.3. 400 °C *to* 600 °C

By 400 °C, the furan peak at 286.6 eV is eliminated, and a shoulder present in the oxygen *K*-edge XRS spectra at 535.3 eV is also removed (Fig. 6). Previous studies have attributed this feature in carbon materials to be due to the presence of **O**=C furan bonding [54,55]. At pyrolysis temperatures exceeding 400 °C, the peak area for the aromatic region of the C *K*-edge spectra increases linearly with temperature. Carbonyl functionalities in the bulk carbon can also be seen to be removed in the 289 eV region (Fig. 5b). The primary mechanism in this temperature range is aromatic condensation. The peak area at 286.6 eV, attributed to C=C–O furan species, remains stable between 350 °C to 500 °C (Fig. 5c), likely due to the formation of a stable intermediate oxygen species. XRS spectra for the same samples recorded at the Oxygen *K*-edge (Fig. 6) show a −0.6 eV shift in the O $1s-\pi^*$ transition energy. A transition at ca. 532 eV is commonly attributed to the **O**=C bonding in similar carbon materials [56–58]. The experimentally observed shift of the O $1s-\pi^*$ transition energy, infers the presence of a more stable C_{arom}-O species at temperatures above 400 °C. The evolved species recorded using pyGCMS (Section 3.2) suggest these species may be quinone or pyran-like carbon functionalities; with oxygen now bonded to C6 aromatic species rather than the furanic 5-membered ring. In order to further investigate the formation of this intermediate, simulated oxygen *K*-edge XRS spectra for three test molecules were performed to identify the observed spectral changes (Supplementary Information S4). The test molecules chosen were: (i) 5-hydroxymethylfurfural (5-HMF) (ii) pyran and (iii) 1,4-napthoquinone (quinone) to represent furan, pyran and quinone-like oxygen functionalities. The 5-HMF structure was chosen to represent the known polyfuran-like structure of the starting hydrothermal carbon [24]. Notably, the calculated spectra reproduce the negative shift (−0.8 eV) in the O $1s-\pi^*$ transition energy observed upon increasing pyrolysis temperature. Furthermore, the removal of the shoulder present at 535.3 eV is also reproduced. Beyond 500 °C, a decrease in the C_{arom}-O peak area is observed. At this stage, the low oxygen abundance within the system makes accurate quantification of O species from the O *K*-edge challenging due to signal-to-noise issues. However, at pyrolysis temperatures above 500 °C, it is expected that all carbonyl-like functionality is removed, and the remaining oxygen is eliminated during the condensation of the aromatic network by the release of carbon oxides.

The mass loss observed by TGA analyses (Fig. 2) in the 400 °C to 600 °C range can be attributed to the release of aromatic hydrocarbon (e.g., toluene) products, as confirmed by pyGCMS. The pyGCMS (Fig. 3) results show that aromatic analytes (e.g., toluene and phenol) start growing around 400 °C and continue to grow beyond 600 °C, while furanic analytes level off by 500 °C and start to decrease by 600 °C. FTIR results (Fig. 4) suggest triplet formation at higher temperatures, likely due to increased amounts of aromatic functionalities. Fig. 5b provides clear evidence of the beginning of the growth of aromatic peaks in the temperature range of 350 °C to 400 °C. The aromatic (285 eV) resonance observed in the C *K*-edge XRS results (Fig. 5a) for pyHTC-600 indicates the evolution of the amorphous carbon structure into a more ordered turbostratic structure, which constitutes the final carbon product. Our O *K*-edge XRS results (Fig. 6) show the low abundance of O in this temperature range, which is consistent with deoxygenation reactions.

Collectively, TGA, pyGCMS, FTIR, C *K*-edge, and O *K*-edge XRS data all point towards (1) release of aromatic hydrocarbon products, (2) growth of aromatic carbon, (3) decrease in furanic carbon, (4) loss of oxygen, and (5) restructuring of pyHTC from amorphous to a more structured material in the 400 °C to 600 °C range. These results are consistent with the aromatisation of cellulose during pyrolysis in a similar temperature range. In cellulose, oxygenated groups are removed from aromatic structures through deoxygenation and dehydrogenation in the temperature range of 400 °C to 600 °C and beyond 650 °C, respectively [59–61]. Our previous results have shown more pronounced aromatisation and graphitisation of pyrolysed oak wood samples at 650 °C [24]. Interestingly, C *K*-edge NEXAFS have provided evidence for a core–shell structure in glucose HTC, with a more condensed core [8]. In contrast, the surface of pyHTC is likely to be more condensed, as evidenced by the pyrolysis of oak wood. We anticipate that future studies will shed further insight into the aromatisation of sugar-based pyHTC beyond 600 °C.

4. Summary

The thermal treatment of biomass-derived hydrothermal carbon is in wide use for improving the properties of carbons produced through hydrothermal carbonisation. The benefits of using hydrothermal carbonisation as an initial treatment (e.g., chemical tunability and the ability to treat wet biomass feedstocks) make the process highly favourable for wider implementation. However, secondary thermal treatment has been shown to induce new and useful chemistry (e.g., surface functionality) and physical properties (e.g., increased porosity, conductivity).

The methodological approach integrating pyGCMS and X-ray Raman Spectroscopy (XRS) introduced in our study has contributed to our understanding of this process in several key ways. Firstly, the combination of pyGCMS and XRS offers a more sensitive investigation of the volatile pyrolysate and solid phase carbon chemistry. While XRS caters to solid phase carbon chemistry, pyGCMS is responsive to volatile pyrolysate. This means that together, these techniques can observe and analyse both solid and gaseous phases of the sample, adding to the completeness and comprehensiveness of the data. Secondly, XRS coupled to pyGCMS allows for the investigation of average chemical changes in carbon bonds without the limitations of other spectroscopic techniques, such as low penetration depths or low sensitivity. Lastly, when used together XRS and pyGCMS enable unparallelled insight into temperature-driven processes in carbon materials which are otherwise extremely challenging to monitor using traditional approaches. For example, whilst XRS is a valuable tool for probing a carbon in an element-specific manner, it is often challenging to discriminate similar functionalities. Coupling pyGCMS with XRS allows for much better understanding of the changes in carbon chemistry occurring within a material. Here, this methodological framework has been instrumental in identifying the thermolytic threshold of polyfuranic linking units within pyrolysed hydrothermal carbon, measured between 300 °C to 350 °C. The ability to accurately monitor and chart the evolution of species as a function of temperatures, including the emergence of furan and aromatic species, is a distinct outcome of our combined approach. This study has also demonstrated that pyrolysis temperatures above 350 °C yield a stable C–O species. Taken together, the combined use of XRS and pyGCMS offers new avenues to explore intricate chemical processes in the thermal treatment of biomass-derived hydrothermal carbon. With the development of more portable mass spectrometry systems, we suggest that the future development of *in situ* XRS-GCMS should be investigated for future research in carbon science, including scalable applications and wider implementation.

CRediT authorship contribution statement

Luke J.R. Higgins: Writing – review & editing, Writing – original draft, Investigation, Formal analysis, Conceptualization, Methodology. **James M. Hammerton:** Writing – review & editing, Investigation, Formal analysis. **Evangeline B. McShane:** Investigation, Formal analysis. **Andrew B. Ross:** Supervision, Resources. **Christoph J. Sahle:** Writing – review & editing, Investigation, Formal analysis, Software. **Bhoopesh Mishra:** Writing – review & editing, Supervision.

Declaration of competing interest

The authors declare that they have no known competing financial interests or personal relationships that could have appeared to influence the work reported in this paper.

Acknowledgements

This work was supported by the Engineering and Physical Sciences Research Council, United Kingdom [EP/L014912/1] and [EP/K014714/1] as part of the UK Centre for Doctoral Training in Bioenergy at the University of Leeds and the UK Catalysis Hub. We acknowledge the European Synchrotron Radiation Facility (ESRF) for provision of synchrotron radiation facilities under proposal number CH6167 and we would like to thank Florent Gerbon and Alessandro Longo for assistance and support in using beamline ID20. Assistance in collection of FTIR data by Dr Adrian Cunliffe is gratefully acknowledged.

Appendix A. Supplementary data

Supplementary material related to this article can be found online at https://doi.org/10.1016/j.jaap.2025.107542.

Data availability

Data will be made available on request.

References

[1] S.A. Nicolae, H. Au, P. Modugno, H. Luo, A.E. Szego, M. Qiao, L. Li, W. Yin, H.J. Heeres, N. Berge, M.M. Titirici, Recent advances in hydrothermal carbonisation: From tailored carbon materials and biochemicals to applications and bioenergy, Green Chem. 22 (2020) 4747–4800, http://dx.doi.org/10.1039/d0gc00998a.

[2] M.M. Titirici, M. Antonietti, Chemistry and materials options of sustainable carbon materials made by hydrothermal carbonization, Chem. Soc. Rev. 39 (2010) 103–116, http://dx.doi.org/10.1039/b819318p.

[3] M.-M. Titirici, Sustainable Carbon Materials from Hydrothermal Processes, John Wiley & Sons, Ltd, Oxford, UK, 2013, http://dx.doi.org/10.1002/9781118622179.

[4] R. Becker, U. Dorgerloh, E. Paulke, J. Mumme, I. Nehls, Hydrothermal carbonization of biomass: Major organic components of the aqueous phase, Chem. Eng. Technol. 37 (2014) 511–518, http://dx.doi.org/10.1002/CEAT.201300401.

[5] A. Ross, A.P. Harvey, A. Goguet, H. Manyar, J. Onwudili, G.P. Deshmukh, K. Zhang, J. Hammerton, Catalytic upgrading of aqueous streams from hydrothermal processing of biomass to higher-value products, in: Modern Developments in Catalysis: Volume 2, vol. 2, World Scientific Publishing Co., 2023, pp. 187–218, http://dx.doi.org/10.1142/9781800612013_0005.

[6] B. Hu, K. Wang, L. Wu, S.H. Yu, M. Antonietti, M.M. Titirici, Engineering carbon materials from the hydrothermal carbonization process of biomass, Adv. Mater. 22 (2010) 813–828, http://dx.doi.org/10.1002/adma.200902812.

[7] A. Singh, M.L. Tsai, C.W. Chen, R. Rani Singhania, A. Kumar Patel, V. Tambat, C.D. Dong, Role of hydrothermal pretreatment towards sustainable biorefinery, Bioresour. Technol. 367 (2023) http://dx.doi.org/10.1016/j.biortech.2022.128271.

[8] L.J. Higgins, A.P. Brown, J.P. Harrington, A.B. Ross, B. Kaulich, B. Mishra, Evidence for a core–shell structure of hydrothermal carbon, Carbon 161 (2020) 423–431, http://dx.doi.org/10.1016/J.CARBON.2020.01.060.

[9] C. Falco, N. Baccile, M.-M. Titirici, Morphological and structural differences between glucose, cellulose and lignocellulosic biomass derived hydrothermal carbons, Green Chem. 13 (2011) 3273, http://dx.doi.org/10.1039/c1gc15742f.

[10] J. Feng, R. Cai, E. Magliocca, H. Luo, L. Higgins, G.L. Romario, X. Liang, A. Pedersen, Z. Xu, Z. Guo, A. Periasamy, D. Brett, T.S. Miller, S.J. Haigh, B. Mishra, M.M. Titirici, Iron, nitrogen co-doped carbon spheres as low cost, scalable electrocatalysts for the oxygen reduction reaction, Adv. Funct. Mater. 31 (2021) http://dx.doi.org/10.1002/adfm.202102974.

[11] N.A. Rashidi, Y.H. Chai, I.S. Ismail, M.F.H. Othman, S. Yusup, Biomass as activated carbon precursor and potential in supercapacitor applications, Biomass Convers. Biorefinery (2022) http://dx.doi.org/10.1007/s13399-022-02351-1.

[12] Z. Xu, J. Wang, Z. Guo, F. Xie, H. Liu, H. Yadegari, M. Tebyetekerwa, M.P. Ryan, Y.S. Hu, M.M. Titirici, The role of hydrothermal carbonization in sustainable sodium-ion battery anodes, Adv. Energy Mater. 12 (2022) http://dx.doi.org/10.1002/aenm.202200208.

[13] F. Trotta, G.J. Wang, Z. Guo, Z. Xu, M. Crespo Ribadeneyra, H. Au, J.S. Edge, M.M. Titirici, L. Lander, A comparative techno-economic and lifecycle analysis of biomass-derived anode materials for lithium- and sodium-ion batteries, Adv. Sustain. Syst. 6 (2022) http://dx.doi.org/10.1002/adsu.202200047.

[14] X. Feng, Y. Bai, M. Liu, Y. Li, H. Yang, X. Wang, C. Wu, Untangling the respective effects of heteroatom-doped carbon materials in batteries, supercapacitors and the ORR to design high performance materials, Energy Environ. Sci. 14 (2021) 2036–2089, http://dx.doi.org/10.1039/d1ee00166c.

[15] Y. Gao, Q. Wang, G. Ji, A. Li, J. Niu, Doping strategy, properties and application of heteroatom-doped ordered mesoporous carbon, RSC Adv. 11 (2021) 5361–5383, http://dx.doi.org/10.1039/D0RA08993A.

[16] A.D. Roberts, X. Li, H. Zhang, Porous carbon spheres and monoliths: Morphology control, pore size tuning and their applications as Li-ion battery anode materials, Chem. Soc. Rev. 43 (2014) 4341–4356, http://dx.doi.org/10.1039/c4cs00071d.

[17] A.A. Burbano, G.A. Medina, F.H. Sánchez, V.L. Lassalle, M.F. Horst, G. Gascó, A. Méndez, Influence of post-pyrolysis treatment on physicochemical properties and acid medium stability of magnetic carbon nanocomposites, Biomass Convers. Biorefinery (2022) http://dx.doi.org/10.1007/s13399-022-03517-7.

[18] S. Zhi, Q. Dai, H. Wang, D. Wu, L. Zhao, C. Hu, L. Dai, Heteroatom-doped carbon materials for multifunctional noncatalytic applications, ACS Nano 19 (2025) 29860–29897, http://dx.doi.org/10.1021/acsnano.5c04478.

[19] I. Matos, M. Bernardo, I. Fonseca, Porous carbon: A versatile material for catalysis, Catal. Today 285 (2017) 194–203, http://dx.doi.org/10.1016/j.cattod.2017.01.039.

[20] W.-J. Liu, H. Jiang, H.-Q. Yu, Emerging applications of biochar-based materials for energy storage and conversion, Energy & Environ. Sci. 12 (2019) 1751–1779, http://dx.doi.org/10.1039/C9EE00206E.

[21] L. Yu, C. Falco, J. Weber, R.J. White, J.Y. Howe, M.-M. Titirici, Carbohydrate-derived hydrothermal carbons: A thorough characterization study, Langmuir 28 (2012) 12373–12383, http://dx.doi.org/10.1021/la3024277.

[22] C. Falco, F. Perez Caballero, F. Babonneau, C. Gervais, G. Laurent, M.-M. Titirici, N. Baccile, Hydrothermal carbon from biomass: Structural differences between hydrothermal and pyrolyzed carbons via 13 C solid state NMR, Langmuir 27 (2011) 14460–14471, http://dx.doi.org/10.1021/la202361p.

[23] R. Georgiou, C.J. Sahle, D. Sokaras, S. Bernard, U. Bergmann, J.P. Rueff, L. Bertrand, X-ray raman scattering: A hard X-ray probe of complex organic systems, Chem. Rev. 122 (2022) 12977–13005, http://dx.doi.org/10.1021/acs.chemrev.1c00953.

[24] L.J.R. Higgins, C.J. Sahle, M. Balasubramanian, B. Mishra, X-ray Raman scattering for bulk chemical and structural insight into green carbon, Phys. Chem. Chem. Phys. 22 (2020) 18435–18446, http://dx.doi.org/10.1039/D0CP00417K.

[25] I. Pastorova, R.E. Botto, P.W. Arisz, J.J. Boon, Cellulose char structure: a combined analytical Py-GC-MS, FTIR, and NMR study, Carbohydr. Res. 262 (1994) 27–47, http://dx.doi.org/10.1016/0008-6215(94)84003-2.

[26] A. Magdziarz, M. Wilk, M. Wądrzyk, Pyrolysis of hydrochar derived from biomass – experimental investigation, Fuel 267 (2020) 117246, http://dx.doi.org/10.1016/J.FUEL.2020.117246.

[27] S. Wang, H. Persson, W. Yang, P.G. Jönsson, Pyrolysis study of hydrothermal carbonization-treated digested sewage sludge using a Py-GC/MS and a bench-scale pyrolyzer, Fuel 262 (2020) 116335, http://dx.doi.org/10.1016/J.FUEL.2019.116335.

[28] I. Güdücü, K. Alper, T. Evcil, K. Tekin, H. Ohtani, S. Karagöz, Effects of hydrothermal carbonization on products from fast pyrolysis of cellulose, J. the Energy Inst. 99 (2021) 299–306, http://dx.doi.org/10.1016/J.JOEI.2021.10.004.

[29] J. Hammerton, L.R. Joshi, A.B. Ross, B. Pariyar, J.C. Lovett, K.K. Shrestha, B. Rijal, H. Li, P.E. Gasson, Characterisation of biomass resources in nepal and assessment of potential for increased charcoal production, J. Environ. Manag. 223 (2018) 358–370, http://dx.doi.org/10.1016/j.jenvman.2018.06.028.

[30] S. Huotari, C.J. Sahle, C. Henriquet, A. Al-Zein, K. Martel, L. Simonelli, R. Verbeni, H. Gonzalez, M.-C. Lagier, C. Ponchut, M. Moretti Sala, M. Krisch, G. Monaco, A large-solid-angle X-ray Raman scattering spectrometer at ID20 of the European synchrotron radiation facility, J. Synchrotron Radiat. 24 (2017) 521–530, http://dx.doi.org/10.1107/S1600577516020579.

[31] C. Sahle, A. Mirone, J. Niskanen, J. Inkinen, M. Krisch, S. Huotari, Planning, performing and analyzing X-ray Raman scattering experiments, J. Synchrotron Radiat. 22 (2015) 400–409, http://dx.doi.org/10.1107/S1600577514027581.

[32] M. Newville, R. Otten, A. Nelson, A. Ingargiola, T. Stensitzki, D. Allan, A. Fox, F. Carter, D. Pustakhod, Y. Ram, C. Deil, A. Beelen, O. Frost, N. Zobrist, G. Pasquevich, A.L.R. Hansen, T. Spillane, S. Caldwell, A. Polloreno, Andrewhannum, J. Zimmermann, J. Borreguero, J. Fraine, B.F. Maier, B. Gamari, A. Almarza, Non-Linear Least-Squares Minimization and Curve-Fitting for Python, Zenodo, 2014, http://dx.doi.org/10.5281/zenodo.11813.

[33] D.A. Outka, J. Stöhr, Curve fitting analysis of near-edge core excitation spectra of free, adsorbed, and polymeric molecules, J. Chem. Phys. 88 (1988) 3539–3554, http://dx.doi.org/10.1063/1.453902.

[34] K.G. Latham, W.M. Dose, J.A. Allen, S.W. Donne, Nitrogen doped heat treated and activated hydrothermal carbon: NEXAFS examination of the carbon surface at different temperatures, Carbon 128 (2018) 179–190, http://dx.doi.org/10.1016/j.carbon.2017.11.072.

[35] K.G. Latham, M.I. Simone, W.M. Dose, J.A. Allen, S.W. Donne, Synchrotron based NEXAFS study on nitrogen doped hydrothermal carbon: Insights into surface functionalities and formation mechanisms, Carbon 114 (2017) 566–578, http://dx.doi.org/10.1016/j.carbon.2016.12.057.

[36] A. Braun, A. Kubatova, S. Wirick, S.B. Mun, Radiation damage from EELS and NEXAFS in diesel soot and diesel soot extracts, J. Electron Spectrosc. Relat. Phenom. 170 (2009) 42–48, http://dx.doi.org/10.1016/j.elspec.2007.08.002.

[37] M.L. Gordon, D. Tulumello, G. Cooper, A.P. Hitchcock, P. Glatzel, O.C. Mullins, S.P. Cramer, U. Bergmann, Inner-shell excitation spectroscopy of fused-ring aromatic molecules by electron energy loss and X-ray Raman techniques, J. Phys. Chem. A 107 (2003) 8512–8520, http://dx.doi.org/10.1021/jp035607r.

[38] A.P. Hitchcock, J. Li, S.R. Reijerkerk, P. Foley, H.D. Stöver, I. Shirley, X-ray absorption spectroscopy of polyureas and polyurethanes and their use in characterizing chemical gradients in thin-walled polyurea capsules, J. Electron Spectrosc. Relat. Phenom. 156–158 (2007) 467–471, http://dx.doi.org/10.1016/j.elspec.2006.11.061.

[39] N. Baccile, G. Laurent, F. Babonneau, F. Fayon, M.-M. Titirici, M. Antonietti, Structural characterization of hydrothermal carbon spheres by advanced solid-state MAS 13 C NMR investigations, J. Phys. Chem. C 113 (2009) 9644–9654, http://dx.doi.org/10.1021/jp901582x.

[40] L.H. Al-Madhagi, S.Y. Chang, M. Balasubramanian, A.B. Kroner, E.J. Shotton, E.A. Willneff, B. Mishra, S.L. Schroeder, X-ray raman scattering: A new: In situ probe of molecular structure during nucleation and crystallization from liquid solutions, CrystEngComm 20 (2018) 6871–6884, http://dx.doi.org/10.1039/c8ce00929e.

[41] J. Stohr, NEXAFS spectroscopy, first ed., in: Springer Series in Surface Sciences, vol. 25, Springer Berlin Heidelberg, Berlin, Heidelberg, 1992, http://dx.doi.org/10.1007/978-3-662-02853-7.

[42] C. Rodriguez Correa, M. Bernardo, R.P. Ribeiro, I.A. Esteves, A. Kruse, Evaluation of hydrothermal carbonization as a preliminary step for the production of functional materials from biogas digestate, J. Anal. Appl. Pyrolysis 124 (2017) 461–474, http://dx.doi.org/10.1016/J.JAAP.2017.02.014.

[43] V. Strezov, M. Patterson, V. Zymla, K. Fisher, T.J. Evans, P.F. Nelson, Fundamental aspects of biomass carbonisation, J. Anal. Appl. Pyrolysis 79 (2007) 91–100, http://dx.doi.org/10.1016/j.jaap.2006.10.014.

[44] C.B. Rasrendra, M. Windt, Y. Wang, S. Adisasmito, I.G. Makertihartha, E.R. Van Eck, D. Meier, H.J. Heeres, Experimental studies on the pyrolysis of humins from the acid-catalysed dehydration of C6-sugars, J. Anal. Appl. Pyrolysis 104 (2013) 299–307, http://dx.doi.org/10.1016/J.JAAP.2013.07.003.

[45] M.P. Olszewski, P.J. Arauzo, M. Wądrzyk, A. Kruse, Py-GC-MS of hydrochars produced from brewer's spent grains, J. Anal. Appl. Pyrolysis 140 (2019) 255–263, http://dx.doi.org/10.1016/j.jaap.2019.04.002.

[46] F. Xia, Z. Du, J. Liu, Y. Ma, J. Xu, Catalytic oxidative C–C bond cleavage route of levulinic acid and methyl levulinate, RSC Adv. 6 (2016) 72744–72749, http://dx.doi.org/10.1039/C6RA16149A.

[47] J. Poerschmann, B. Weiner, R. Koehler, F.D. Kopinke, Hydrothermal carbonization of glucose, fructose, and xylose - Identification of organic products with medium molecular masses, ACS Sustain. Chem. Eng. 5 (2017) 6420–6428, http://dx.doi.org/10.1021/acssuschemeng.7b00276.

[48] P.T. Williams, S. Besler, The influence of temperature and heating rate on the slow pyrolysis of biomass, Renew. Energy 7 (1996) 233–250, http://dx.doi.org/10.1016/0960-1481(96)00006-7.

[49] C. Rodriguez Correa, T. Hehr, A. Voglhuber-Slavinsky, Y. Rauscher, A. Kruse, Pyrolysis vs. hydrothermal carbonization: Understanding the effect of biomass structural components and inorganic compounds on the char properties, J. Anal. Appl. Pyrolysis 140 (2019) 137–147, http://dx.doi.org/10.1016/j.jaap.2019.03.007.

[50] M. Sevilla, L. Yu, C.O. Ania, M.M. Titirici, Supercapacitive behavior of two glucose-derived microporous carbons: Direct pyrolysis versus hydrothermal carbonization, ChemElectroChem (2014) http://dx.doi.org/10.1002/celc.201402233.

[51] Y. Lin, H. Xu, Y. Gao, X. Zhang, Preparation and characterization of hydrochar-derived activated carbon from glucose by hydrothermal carbonization, Biomass Convers. Biorefinery (2023) 3785–3796, http://dx.doi.org/10.1007/s13399-021-01407-y/Published.

[52] P. Modugno, M.M. Titirici, Influence of reaction conditions on hydrothermal carbonization of fructose, ChemSusChem 14 (2021) 5271–5282, http://dx.doi.org/10.1002/CSSC.202101348.

[53] R. Galaverna, M.C. Breitkreitz, J.C. Pastre, Conversion of d -fructose to 5-(hydroxymethyl)furfural: Evaluating batch and continuous flow conditions by design of experiments and in-line FTIR monitoring, ACS Sustain. Chem. Eng. 6 (2018) 4220–4230, http://dx.doi.org/10.1021/acssuschemeng.7b04643.

[54] J.L. Solomon, R.J. Madix, J. Stöhr, Orientation and absolute coverage of furan and 2 5-dihydrofuran on ag(110) determined by near edge X-ray absorption fine structure and X-ray photoelectron spectroscopy, J. Chem. Phys. 94 (1991) 4012–4023, http://dx.doi.org/10.1063/1.460678.

[55] M.J. Knight, F. Allegretti, E.A. Kröger, M. Polcik, C.L.A. Lamont, D.P. Woodruff, The adsorption structure of furan on Pd(111), Surf. Sci. 602 (2008) 2524–2531, http://dx.doi.org/10.1016/j.susc.2008.05.041.

[56] Y. Dang, Y. Liu, P. Xiang, Z. Tan, Z. Tian, M. Greiner, S. Heumann, Y. Ding, Z.-A. Qiao, Carbon surface chemistry: Benchmark for the analysis of oxygen functionalities on carbon materials, Adv. Mater. 37 (2025) 2418239, http://dx.doi.org/10.1002/adma.202418239.

[57] J. Zhou, P. Yang, P.A. Kots, M. Cohen, Y. Chen, C.M. Quinn, M.D. de Mello, J.A. Boscoboinik, W.J. Shaw, S. Caratzoulas, W. Zheng, D.G. Vlachos, Tuning the reactivity of carbon surfaces with oxygen-containing functional groups, Nat. Commun. 14 (2023) 2293, http://dx.doi.org/10.1038/s41467-023-37962-3.

[58] H.W. Kim, M.B. Ross, N. Kornienko, L. Zhang, J. Guo, P. Yang, B.D. McCloskey, Efficient hydrogen peroxide generation using reduced graphene oxide-based oxygen reduction electrocatalysts, Nat. Catal. 1 (2018) 282–290, http://dx.doi.org/10.1038/s41929-018-0044-2.

[59] Y.-C. Lin, J. Cho, G.A. Tompsett, P.R. Westmoreland, G.W. Huber, Kinetics and mechanism of cellulose pyrolysis, J. Phys. Chem. C 113 (2009) 20097–20107, http://dx.doi.org/10.1021/jp906702p.

[60] X. Yang, Z. Fu, D. Han, Y. Zhao, R. Li, Y. Wu, Unveiling the pyrolysis mechanisms of cellulose: Experimental and theoretical studies, Renew. Energy 147 (2020) 1120–1130, http://dx.doi.org/10.1016/j.renene.2019.09.069.

[61] H. Kawamoto, Review of reactions and molecular mechanisms in cellulose pyrolysis, Curr. Org. Chem. 20 (2016) 2444–2457, http://dx.doi.org/10.2174/1385272820666160525102910.